Research Square

Preprints are preliminary reports that have not undergone peer review.
They should not be considered conclusive, used to inform clinical practice,
or referenced by the media as validated information.

Targeting the ELAVL1-HMGCR axis disrupts lipid-droplet buffering and promotes lipotoxic cell death in colorectal cancer

Lan Liu

lliugi@whu.edu.cn

Zhongnan Hospital of Wuhan University, Wuhan, China https://orcid.org/0000-0002-7394-6011

Fengxing Huang

Zhongnan Hospital of Wuhan University

Yu Shao

Zhongnan Hospital of Wuhan University

Youwei Wang

Zhongnan Hospital of Wuhan University

Runan Zhang

Zhongnan Hospital of Wuhan University https://orcid.org/0000-0003-2366-4195

Mengting Li

Zhongnan Hospital of Wuhan University

Kun Lin

https://orcid.org/0000-0002-8572-9479

Hong Yang

Peking Union Medical College Hospital

Qiu Zhao

Zhongnan Hospital of Wuhan University https://orcid.org/0000-0002-1596-5505

Article

Keywords: Lipid Droplets (LDs), ELAVL1, Post-transcriptional Regulation, Lipotoxic Cell Death, Colorectal Cancer (CRC)

Posted Date: November 11th, 2026

DOI: https://doi.org/10.21203/rs.3.rs-10377613/v1

License: This work is licensed under a Creative Commons Attribution 4.0 International License.
Read Full License

Additional Declarations: (Not answered)

Targeting the ELAVL1-HMGCR axis disrupts lipid-droplet buffering and promotes lipotoxic cell death in colorectal cancer

Fengxing Huang[1, 2, 3, *], Yu Shao[1, 2, *], Youwei Wang[1, 2], Runan Zhang[1, 2], Kun Lin[1, 2], Mengting Li[1, 2], Hong Yang[4 #], Qiu Zhao[1, 2, #], and Lan Liu[1, 2, #]

[1] Department of Gastroenterology, Zhongnan Hospital of Wuhan University, Wuhan, 430071, China.

[2] Hubei Clinical Center and Key Lab of Intestinal and Colorectal Diseases, Wuhan, 430071, China.

[3] National Clinical Research Center for Digestive Diseases, Department of Gastroenterology, Changhai Hospital, Naval Medical University, Shanghai, 200433, China.

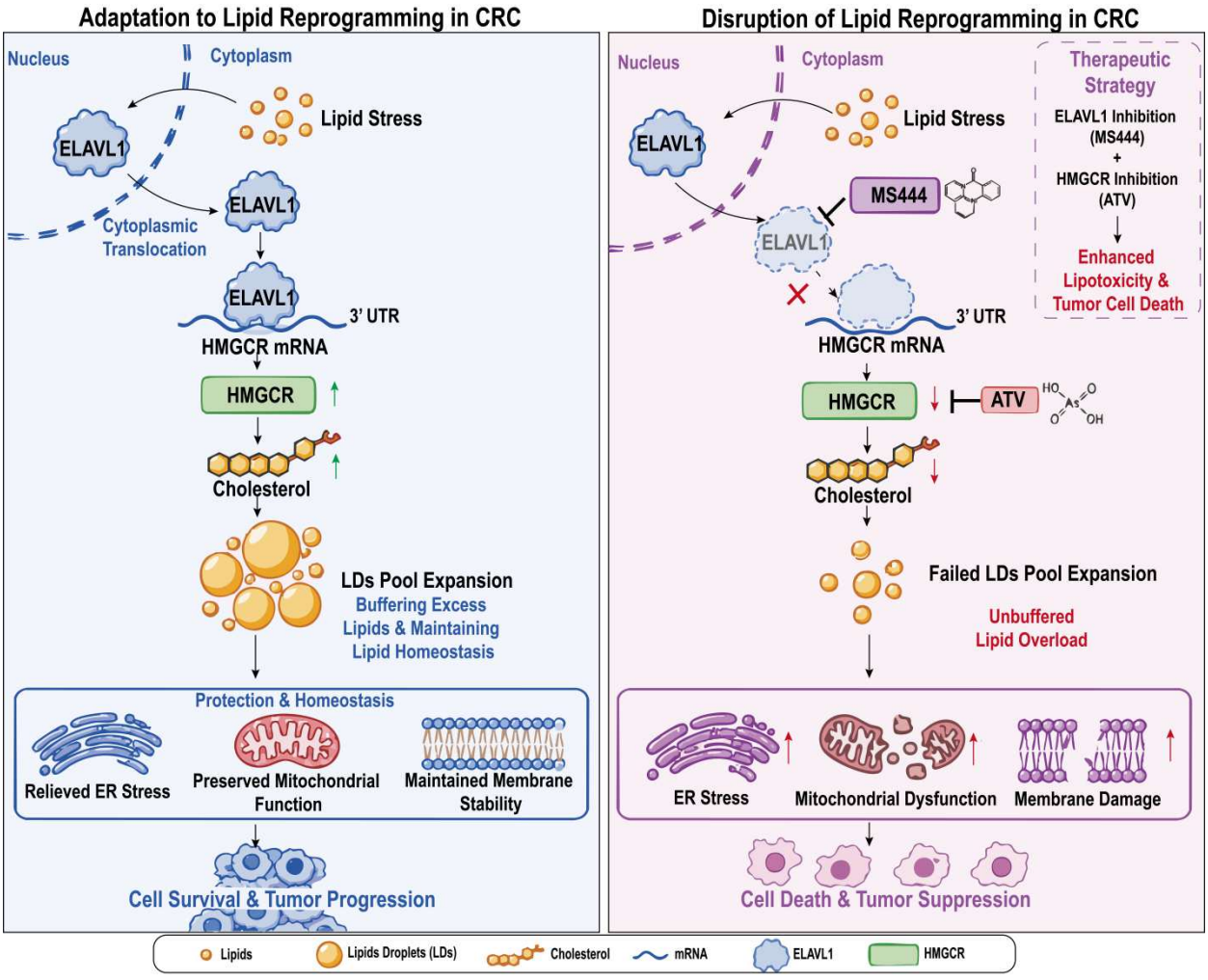
[4] Department of Gastroenterology, Peking Union Medical College Hospital, Chinese Academy of Medical Sciences & Peking Union Medical College, Beijing, 100730, China.

[*] These authors contributed equally to this study.

[#] Correspondence: Hongy72@163.com (Hong Yang), qiuzhao@whu.edu.cn (Qiu Zhao), lliugi@whu.edu.cn (Lan Liu).

ABSTRACT

Lipid metabolic reprogramming is a key feature of colorectal cancer (CRC), yet how CRC cells tolerate lipid overload and evade lipotoxic cell death remains incompletely understood. This study reveals that the ELAVL1/HMGCR/lipid-droplet axis supports CRC cell survival under lipid-rich conditions. Fatty-acid exposure, high-fat diet, and tumor-associated metabolic remodeling promoted cytoplasmic translocation of the RNA-binding protein ELAVL1, accompanied by lipid droplet accumulation in CRC. ELAVL1 depletion impaired triglyceride and cholesterol ester storage, reduced lipid-droplet biogenesis, and sensitized CRC cells to endoplasmic reticulum stress, mitochondrial fragmentation, membrane damage, reactive oxygen species accumulation, and apoptosis. Conversely, ELAVL1 overexpression enhanced neutral-lipid storage and protected cells from lipotoxic damage. Mechanistically, ELAVL1 binds the 3′UTR of HMGCR mRNA and enhances its stability, thereby maintaining the cholesterol/mevalonate pathway. In ELAVL1-deficient cells, restoration of HMGCR rescued lipid droplet formation, lipid homeostasis, and organelle integrity, whereas inhibition of HMGCR abolished ELAVL1-driven lipid droplet expansion and cytoprotective effects. In high-fat-diet-associated CRC models, ELAVL1 inhibition suppressed lipid-droplet accumulation, whereas combined ELAVL1/HMGCR targeting disrupted lipid homeostasis, enhanced apoptosis, and reduced tumor burden. These findings suggest that ELAVL1-mediated stabilization of HMGCR mRNA promotes lipid-droplet buffering, thereby protecting CRC cells from lipotoxic cell death, and point to a targetable vulnerability in colorectal cancer therapy.



KEYWORDS:

Lipid Droplets (LDs), ELAVL1, Post-transcriptional Regulation, Lipotoxic Cell Death, Colorectal Cancer (CRC)

INTRODUCTION

Lipid metabolic reprogramming is increasingly recognized as a critical hallmark of colorectal cancer (CRC)[1,2]. Cancer cells typically increase lipid uptake, de novo lipid synthesis, cholesterol biosynthesis, and lipid remodeling to support rapid proliferation, membrane biosynthesis, redox balance, and adaptation to the tumor microenvironment[3]. In CRC, abnormalities in lipid metabolism are closely associated with obesity, high-fat diets, tumor progression, metastasis, and treatment resistance. However, lipid accumulation is a double-edged sword. While an increased supply of lipids provides metabolic substrates for tumor growth, excessive fatty acids and cholesterol-derived metabolites can disrupt cell membrane composition, induce oxidative stress, impair organelle function, and trigger lipotoxic cell death[4,5]. Emerging evidence indicates that lipid metabolic reprogramming in CRC not only facilitates tumorigenesis but also sustains tumor progression by balancing lipid synthesis and degradation[6–8]. Therefore, CRC cells must develop adaptive mechanisms that enable them to utilize a lipid-rich environment while avoiding cell damage caused by lipid overload.

Lipotoxic stress affects multiple cellular compartments. Saturated fatty acids (such as palmitic acid) disrupt endoplasmic reticulum (ER) membrane homeostasis, promote ER stress, increase reactive oxygen species (ROS) production, and impair mitochondrial integrity[9]. Dysregulation of lipid metabolism also alters plasma membrane structure and increases cellular sensitivity to apoptotic signals. These processes indicate that lipid metabolic adaptation is not only a biosynthetic process but also a cellular survival mechanism that determines whether cancer cells tolerate lipid overload or undergo cell death. Although growing evidence suggests that lipid metabolism is associated with the

progression of CRC, the molecular pathways linking lipid stress to organelle protection and resistance to cell death remain incompletely elucidated.

Lipid droplets (LDs) are dynamic intracellular organelles composed of a neutral lipid core, a phospholipid monolayer, and associated proteins[10–13]. Traditionally, LDs were considered passive lipid reservoirs, but it is now recognized that they are also active regulators of lipid transport, energy metabolism, redox homeostasis, membrane remodeling, and cellular stress responses[14,15]. By sequestering excess free fatty acids and cholesterol, LDs mitigate lipotoxicity, reduce ER stress, and prevent oxidative damage. In cancer, the accumulation and metabolism of LDs are closely associated with metabolic plasticity, survival under nutritional or oxidative stress, treatment resistance, and invasive tumor behavior[16–20]. However, how LD biosynthesis is regulated under lipid-rich conditions in CRC, and whether LDs are directly involved in protecting CRC cells from lipotoxic cell death, remain important unresolved questions.

ELAVL1 (also known as HuR) is an RNA-binding protein that regulates post-transcriptional gene expression by stabilizing and/or promoting the translation of target mRNAs[21–23]. Under normal conditions, ELAVL1 is primarily located in the cell nucleus; however, in response to cellular stress, it translocates to the cytoplasm, where it regulates the expression of various oncogenes and stress-response genes[24,25]. Elevated cytoplasmic ELAVL1 has been associated with poor prognosis and aggressive tumor behavior in various cancers[26]. Our previous studies have confirmed that ELAVL1 is a key sensor and regulator of lipid metabolism in CRC[27]. Recent studies suggest that ELAVL1 may also regulate lipid metabolism[28], but its role in lipid droplet formation and lipid homeostasis in CRC remains unclear.

In this study, we investigated whether ELAVL1 controls CRC cell survival under lipid overload by regulating HMGCR-dependent LD formation. We demonstrate that lipid stress induced by fatty-acid exposure, high-fat diet, or tumor-associated metabolic remodeling promotes cytoplasmic accumulation of ELAVL1 and LD enrichment in CRC. Mechanistically, ELAVL1 directly binds the 3′UTR of HMGCR mRNA and increases its stability, thereby sustaining HMGCR expression and cholesterol/mevalonate-pathway activity. Disruption of the ELAVL1/HMGCR axis impairs LD biogenesis, aggravates ER stress, mitochondrial damage, membrane injury, oxidative stress, and apoptosis, whereas HMGCR restoration rescues lipid homeostasis and organelle integrity. Finally, pharmacological targeting of ELAVL1, especially in combination with HMGCR inhibition, suppresses lipid-driven CRC progression in vivo. These findings define the ELAVL1/HMGCR/LD axis as a post-transcriptional lipid-stress adaptation mechanism that protects CRC cells from lipotoxic cell death and may represent a therapeutically actionable vulnerability in colorectal cancer.

RESULTS

1. Lipid stress induces cytoplasmic ELAVL1 accumulation and LD enrichment during CRC progression

To explore whether ELAVL1 responds to lipid metabolic stress, we treated CRC cell lines (HT29, HCT116, RKO) with palmitic acid (PA, 200 μM, 24 h). PA was used mainly as a lipotoxic saturated fatty-acid stressor, whereas OA was used as an LD-inducing unsaturated fatty acid condition. Cells with higher baseline ELAVL1 expression (HT29)

exhibited greater tolerance to PA-induced stress, whereas those with lower ELAVL1 (RKO) were more susceptible **(Fig. S1A, S1B)**. Subcellular fractionation revealed a consistent redistribution of ELAVL1 from the nucleus to the cytoplasm upon PA or oleic acid (OA) treatment **(Fig. 1A–C, Fig. S1C, S1D)**, suggesting that lipid stress triggers ELAVL1 activation via cytoplasmic translocation. To assess the metabolic consequences, we performed untargeted lipidomics in HT29 cells following ELAVL1 knockdown (shELAVL1) or overexpression (Lv-ELAVL1). ELAVL1 overexpression significantly increased triglycerides (TG), cholesterol esters (CE), and phospholipids **(Fig. 1D–G, Fig. S1E–S1H)**. Differentially expressed metabolites analysis highlighted upregulation of neutral lipid and steroid hormone biosynthesis, with TG showing the most pronounced change **(Fig. 1E)**. Next, we validated these findings in human tissues. Reanalysis of published metabolomics datasets[29] (n = 12) revealed a stepwise increase in TG levels from normal mucosa to CRC, with some adjacent nontumor tissues exhibiting intermediate levels **(Fig. 1H)**. Immunostaining of tissue microarrays showed parallel increases in the lipid droplet marker TIP47 and cytoplasmic ELAVL1 across the adenoma–carcinoma transition **(Fig. 1I–J, Fig. S1I–S1N)**. To validate these associations in vivo, we utilized two CRC mouse models: HFD+AOM and HFD+AOM/DSS. Tumors in both models exhibited elevated ELAVL1 protein levels and distinct cytoplasmic localization, which was closely correlated with TIP47 expression **(Fig. 1K–O, Fig. S2)**. WB analysis further confirmed upregulation of ELAVL1 and lipogenic enzymes (e.g., HMGCR, ACSL1) and decreased expression of pro-apoptotic markers (BAX) in tumor tissues **(Fig. S2G, S2H)**.

Overall, these data indicate that a lipid-rich environment induces the accumulation of ELAVL1 in the cytoplasm of CRC cells and links ELAVL1 activation to LD enrichment, suggesting the existence of a potential adaptive response that protects tumor cells from stress caused by lipid overload.

2. ELAVL1 protects CRC cells from lipid-overload-induced organelle injury and apoptosis

To determine whether ELAVL1 plays a functional role in lipid droplet biosynthesis and intracellular lipid homeostasis, we performed lipidomics and RNA-seq analyses on HT29 cells in which ELAVL1 was knocked down. These analyses revealed a synergistic downregulation of cholesterol ester and phospholipid biosynthetic pathways **(Fig. 2A, 2B)**. Absolute quantification revealed reductions in phosphatidylethanolamine (PE), phosphatidylcholine (PC), phosphatidylserine (PS), and diacylglycerol, indicating that ELAVL1 reprograms lipid synthesis and membrane remodeling. In a subcutaneous xenograft model, Oil Red O staining showed that ELAVL1 knockdown significantly reduced tumor growth and intracellular neutral lipids **(Fig. 2C)**. To further evaluate the role of ELAVL1 in a more physiologically relevant context, we employed the AOM/DSS-induced tumor model using $ELAVL1^{fl/fl}$ and $ELAVL1^{fl/fl\text{-}Villin\text{-}Cre}$ mice. We observed that ELAVL1 deficiency led to a significant reduction in body weight during the induction period **(Fig. 2D)**. Macroscopic examination and statistical analysis revealed that cKO mice developed fewer and smaller colonic tumors compared to $ELAVL1^{fl/fl}$ mice **(Fig. 2E)**. Histological analysis via H&E and Oil Red O staining confirmed that the absence of ELAVL1 suppressed tumor progression and depleted neutral lipid accumulation in vivo

(Fig. 2F). Mass spectrometry confirmed decreases in TG and CE levels in shELAVL1 cells, while Lv-ELAVL1 had the opposite effect **(Fig. 2G, 2H)**. Immunofluorescence further validated these changes at the single-cell level **(Fig. 2I–L)**.

We next investigated whether LD accumulation confers a survival advantage under lipotoxic stress. Electron microscopy revealed extensive mitochondrial fragmentation in shELAVL1 cells, which was exacerbated by PA treatment **(Fig. S3A, S3B)**. In contrast, Lv-ELAVL1 preserved mitochondrial architecture and reduced ROS accumulation **(Fig. S3A–S3D)**. Cell membrane staining and EM further showed that ELAVL1 depletion aggravated membrane structural abnormalities under PA-induced lipid overload **(Figure 2M, 2N)**, consistent with impaired lipid homeostasis and increased cellular stress. Together with mitochondrial damage and ROS accumulation, these findings suggest that ELAVL1-dependent LD accumulation helps preserve organelle and membrane integrity under lipotoxic stress. Accordingly, shELAVL1 cells exhibited reduced proliferation and increased apoptosis, while Lv-ELAVL1 cells were more resistant to PA-induced stress **(Fig. 2O, Fig. S3E–S3H)**. Together, these findings suggest that ELAVL1-dependent LD accumulation is not merely a metabolic phenotype, but rather a cellular protective mechanism that maintains organelle and membrane integrity and limits lipotoxic apoptosis in CRC cells.

3. ELAVL1 promotes lipid droplet biogenesis and cholesterol-related biosynthesis centered on HMGCR

To identify the metabolic pathways downstream of ELAVL1, we analyzed transcriptomic and lipidomic changes associated with ELAVL1 loss. Among the 1,328 differentially expressed genes, several cholesterol and lipid metabolism pathways were significantly enriched **(Fig. 3A, 3B)**. Notely, genes involved in cholesterol biosynthesis, including HMGCR, are important downstream effectors of ELAVL1 **(Fig. 3C)**. Analysis of clinical samples from Zhongnan Hospital further indicates that high ELAVL1 expression is associated with elevated levels of HMGCR and SOAT1 **(Fig. 3D)**. WB and qPCR analyses confirmed that ELAVL1 regulates the expression of HMGCR and other lipogenic enzymes (DGAT1, DHCR7, SOAT1) as well as lipid droplet-associated proteins (PLIN2, ATGL) **(Fig. 3E-G)**. Untargeted lipidomics analysis revealed that ELAVL1 knockdown reduced the levels of specific cholesterol esters (CE 15:0, CE 16:3) and cholesterol derivatives, whereas ELAVL1 overexpression increased the levels of dehydroepiandrosterone sulfate and other cholesterol-related metabolites **(Fig. 3H)**. To further characterize the impact of ELAVL1 on lipid homeostasis, we performed label-free live-cell imaging using Nanolive technology to track the dynamic changes in LDs in Lv-NC and Lv-ELAVL1 cells for up to 12 hours. Representative images show a significant increase in LD content within ELAVL1-overexpressing cells. Morphometric analysis at the single-cell level confirmed the significant increase in lipid droplet number, indicating that ELAVL1 plays a functional role in promoting intracellular lipid droplet accumulation **(Fig. 3I)**. Collectively, these results place ELAVL1 upstream of a cholesterol biosynthetic program that promotes LD expansion, with HMGCR emerging as a key candidate effector.

4. ELAVL1 directly stabilizes HMGCR mRNA to sustain LD buffering under lipid stress

We next investigated whether HMGCR is a direct post-transcriptional target through which ELAVL1 promotes LD biogenesis. Among 43 high-confidence ELAVL1-bound transcripts, HMGCR ranked among the top hits based on peak intensity and fold enrichment **(Fig. 4A)**. ELAVL1 knockdown significantly reduced both HMGCR protein and mRNA levels **(Fig. 4B, 4C)**. Integrated RIP-seq and transcriptomic analyses identified HMGCR as a high-confidence ELAVL1-bound transcript and a candidate mediator of the lipid-storage phenotype. Actinomycin D chase assays revealed that HMGCR mRNA half-life decreased from 8 hours in control cells to 2 hours upon ELAVL1 depletion **(Fig. 4D)**, indicating that ELAVL1 stabilizes HMGCR transcript. RIP-qPCR confirmed specific enrichment of HMGCR mRNA in ELAVL1 immuno-precipitates **(Fig. 4E)**. RNA pull-down assays further demonstrated that ELAVL1 selectively bound to the 3′UTR of HMGCR mRNA, but not to the 5′UTR or coding sequence (CDS) **(Fig. 4F)**. To determine whether HMGCR mediates the effects of ELAVL1 on lipid metabolism, we performed epistasis experiments. HMGCR overexpression in shELAVL1 cells restored TG and TC levels, whereas HMGCR knockdown in Lv-ELAVL1 cells abolished the increase in neutral lipids **(Fig. 4G)**. Immunofluorescence showed that HMGCR re-expression rescued LD number and size in ELAVL1-depleted cells **(Fig. 4H, 4I)**. Untargeted lipidomics identified 14 metabolites that tracked concordantly with HMGCR expression, including saturated TGs (TG 48:0, 50:0), phosphatidylcholine (PC 36:0), and cholesteryl stearate (CE 18:0) **(Fig. 4J–L)**. To further validate the ELAVL1/HMGCR regulatory axis, we utilized Nanolive holotomographic microscopy to monitor LD alterations in Lv-NC and Lv-ELAVL1 cells in

the presence or absence of ATV. In agreement with our prior findings, ATV treatment significantly attenuated the ELAVL1-mediated elevation of LD numbers. This pharmacological attenuation supports the involvement of HMGCR activity in ELAVL1-mediated lipid droplet biogenesis **(Fig. 4M).** These results establish HMGCR mRNA stabilization as a direct post-transcriptional mechanism by which ELAVL1 sustains LD buffering and lipid-stress tolerance in CRC cells.

5. The ELAVL1–HMGCR axis prevents lipotoxic organelle damage and apoptosis

We subsequently investigated whether the ELAVL1–HMGCR axis is causally linked to the proliferative and cytoprotective phenotypes observed. ELAVL1 overexpression enhanced cell proliferation, while atorvastatin (ATV), an HMGCR inhibitor, significantly reduced viability **(Fig. 5A)**. ELAVL1 overexpression partially attenuated ATV-induced cytotoxicity, suggesting that ELAVL1 may buffer statin-induced metabolic stress, potentially through both HMGCR-dependent and HMGCR-independent mechanisms. Apoptosis assays showed that ATV increased cell death in control cells, but this effect was attenuated in ELAVL1-overexpressing cells **(Fig. 5B)**. Bidirectional rescue experiments confirmed that HMGCR is genetically downstream of ELAVL1. shELAVL1 reduced protein levels of HMGCR, SOAT1, DGAT1, DHCR7, CPT1A, ATGL, and PLIN2; these effects were reversed by HMGCR re-expression **(Fig. 5C, 5D)**. In contrast, knocking down HMGCR in Lv-ELAVL1 cells eliminated the associated upregulation of lipases. Electron microscopy revealed that shELAVL1 caused endoplasmic reticulum dilation and mitochondrial fragmentation, and co-knocking down HMGCR exacerbated

these phenomena **(Fig. 5E, 5F)**. Membrane staining showed cholesterol depletion and phosphatidylserine externalization in double-knockdown cells **(Fig. 5G, 5H)**. Re-expression of HMGCR restored ER morphology, mitochondrial integrity, and membrane cholesterol levels. In summary, the ELAVL1–HMGCR axis sustains cholesterol and TG flux, preserves ER, mitochondrial, and membrane homeostasis and thereby suppresses apoptosis under lipid stress.

6. Combined targeting of ELAVL1 and HMGCR disrupts lipid homeostasis and suppresses lipid-driven CRC

We finally examined whether simultaneous inhibition of ELAVL1 and HMGCR could therapeutically disrupt LD-dependent lipid homeostasis in vivo. In the HFD+AOM model, mice developed extensive distal colon tumors and significant weight gain. Treatment with the ELAVL1 inhibitor MS-444 reduced tumor incidence and restored glandular architecture **(Fig. 6A–D)**. Combination therapy (MS-444 + ATV) markedly reduced tumor formation compared with MS-444 alone **(Fig. 6C, 6D)**. Immunostaining and IHC showed that MS-444 significantly reduced ELAVL1 and TIP47 expression **(Fig. 6E, 6F)**. Western blot analysis confirmed downregulation of ELAVL1, HMGCR, ACSL1, and DGAT1 in MS-444-treated groups, with additional suppression of SOAT1 and induction of cleaved caspase-3 in the combination group **(Fig. 6G, 6H)**. Tissue lipidomics revealed significant reductions in TG and TC levels in both MS-444 and combination groups **(Fig. 6I)**.

Consistent with the in vitro findings, dual targeting produced a more profound suppression of tumor burden and lipid accumulation in independent diet-driven CRC models (HFD+AOM/DSS model). Co-treatment with MS-444 and ATV reduced tumor burden and selectively depleted TG and cholesteryl ester species **(Fig. S4)**. Together, these findings indicate that combined disruption of ELAVL1-mediated mRNA stabilization and HMGCR-dependent lipid remodeling collapses LD-based lipid buffering, enhances apoptosis, and suppresses lipid-driven CRC progression in vivo.

DISCUSSION

In this study, we identify a post-transcriptional lipid-stress adaptation mechanism that enables CRC cells to survive lipid overload. We show that lipid-rich conditions, including fatty-acid exposure, high-fat diet, and tumor-associated metabolic remodeling, induce cytoplasmic accumulation of ELAVL1. ELAVL1 directly binds the 3'UTR of HMGCR mRNA and increases its stability, thereby sustaining HMGCR expression, cholesterol/mevalonate-pathway activity, and LD biogenesis. Functionally, this pathway buffers excess lipids and protects CRC cells from ER stress, mitochondrial injury, membrane damage, oxidative stress, and apoptosis. Conversely, disruption of the ELAVL1/HMGCR axis collapses LD-based lipid buffering and sensitizes CRC cells to lipotoxic cell death. These findings define the ELAVL1/HMGCR/LD axis as an adaptive survival program in lipid-driven CRC.

A key implication of our findings is that LD accumulation in CRC should not be viewed simply as a passive marker of altered lipid metabolism. Instead, LDs appear to act as stress-buffering organelles that determine whether lipid-overloaded tumor cells survive or die. Excessive fatty acids and cholesterol-derived metabolites disrupt cell membrane composition, promote endoplasmic reticulum stress, impair mitochondrial integrity, and increase oxidative damage. LDs reduce lipotoxic stress and maintain organelle homeostasis by converting potentially toxic lipid intermediates into neutral lipid stores. Our data support this view: ELAVL1 deficiency reduces the storage of cholesterol esters, impairs LD formation, and exacerbates palmitic acid-induced endoplasmic reticulum stress, mitochondrial fragmentation, cell membrane damage, reactive oxygen species accumulation, and apoptosis; whereas ELAVL1 overexpression enhances the storage of neutral lipids and protects cells from lipotoxic damage. Therefore, the expansion of LDs represents an adaptive cellular protective response of colorectal cancer cells in a lipid-rich environment.

ELAVL1, an RNA-binding protein, has been extensively studied for its ability to regulate oncogenic transcripts involved in cell proliferation, invasion, stress responses, and treatment resistance[30–34]. Our study expands this paradigm by demonstrating that ELAVL1 also regulates lipid stress adaptation in CRC. Importantly, lipid stress not only alters the total abundance of ELAVL1 but also persistently increases the cytoplasmic-to-nuclear ELAVL1 ratio, suggesting that its post-transcriptional regulatory function is activated[35,36]. Changes in ELAVL1 expression and its subcellular localization are implicated in various diseases[37]. This distinction is relevant because cytoplasmic ELAVL1 is generally considered the active pool responsible for target mRNA stabilization and

translational regulation. Lipid homeostasis is maintained through complex regulatory mechanisms involving lipid synthesis, breakdown, transport, and signaling[38,39]. Disruption of lipid balance can lead to cytotoxicity and increased cellular stress[40–43]. High levels of basal ELAVL1 expression were observed to be associated with greater resistance to PA-induced cytotoxicity, further supporting the functional role of ELAVL1 in lipid tolerance. These findings suggest that cytoplasmic ELAVL1 may act as a metabolic stress-responsive RNA regulator, enabling CRC cells to adapt to lipid overload.

Mechanistically, we identify HMGCR as a direct and functional effector of ELAVL1. As the rate-limiting enzyme in the mevalonate pathway, HMGCR is essential for de novo cholesterol synthesis—a process frequently upregulated in cancer to support membrane biogenesis and oncogenic signaling[44–46]. This study demonstrates that ELAVL1 directly binds the HMGCR 3'UTR and stabilizes HMGCR mRNA. By stabilizing HMGCR mRNA, ELAVL1 maintains cholesterol biosynthesis and lipid remodeling, thereby creating the necessary conditions for LD expansion. This positions ELAVL1 upstream of a metabolic program that couples cholesterol synthesis with lipid sequestration and cell protection. Our results further indicate that LDs are a key downstream outcome of ELAVL1/HMGCR activation and a functional determinant of cell fate. When ELAVL1 or HMGCR is inhibited, this protective buffering system breaks down: LD formation decreases, intracellular lipid homeostasis is disrupted, organelle damage increases, and apoptosis is enhanced. Therefore, ELAVL1-driven LD biosynthesis acts as a cytoprotective barrier, preventing cell membrane breakdown and maintaining mitochondrial bioenergetic capacity. The disease context is important. Obesity, high-fat diet, and lipid-rich tumor microenvironments are increasingly linked to CRC progression and poor outcomes.

Tumors growing under these conditions may be particularly dependent on mechanisms that buffer lipid overload and prevent lipotoxic cell death. Our findings suggest that cytoplasmic ELAVL1 and HMGCR expression may help identify CRC tumors with enhanced LD-dependent lipid-stress adaptation. Therapeutically, targeting this pathway may be most relevant in lipid-enriched CRC or in tumors with high cytoplasmic ELAVL1 activity.

Our findings highlight the ELAVL1/HMGCR/LD pathway as a therapeutically actionable metabolic vulnerability in CRC, particularly in lipid-rich settings such as obesity or high-fat-diet-associated disease. Because HMGCR is pharmacologically targetable (via atorvastatin, ATV)[47] and ELAVL1 inhibition further weakens the adaptive response upstream, combined targeting may represent an effective strategy to disrupt lipid homeostasis and induce tumor cell death. More broadly, this work expands the understanding of how RNA-binding proteins shape tumor metabolism by controlling selective metabolic nodes at the mRNA level. Future studies should explore the pharmacokinetics, safety, and optimal dosing of this combination, as well as its potential integration with immunotherapy or dietary interventions.

Several limitations should be considered. First, although our data identify HMGCR as a direct ELAVL1 target and a key mediator of LD formation, the precise metabolic route linking HMGCR-dependent cholesterol/mevalonate-pathway activity to triglyceride-rich LD expansion remains to be fully defined. Isotope tracing experiments and pathway-specific rescue studies are crucial for elucidating this relationship. Second, ELAVL1 is a multifunctional RNA-binding protein, and other transcripts regulated by ELAVL1 may also

be involved in lipid homeostasis. Third, the upstream signaling events driving ELAVL1 cytoplasmic translocation under lipid stress remain unclear. Fourth, although combined targeting of ELAVL1 and HMGCR produced a stronger antitumor effect in vivo, a formal pharmacological synergy has not yet been established. Finally, further validation is needed in patient-derived organoids, xenograft models, larger clinical cohorts, and clinically relevant lipid-rich colorectal cancer models to determine the translational value of this pathway.

In summary, our study reveals that ELAVL1-mediated stabilization of HMGCR mRNA promotes lipid droplet buffering, thereby protecting CRC cells from lipotoxic cell death. The ELAVL1/HMGCR/LD axis links lipid stress, post-transcriptional regulation, cholesterol/mevalonate pathway activity, organelle integrity, and resistance to apoptosis, providing a mechanistic framework for understanding how CRC cells survive under lipid overload. These findings establish the ELAVL1/HMGCR/lipid droplet pathway as a central metabolic survival mechanism in CRC and provide a theoretical basis for therapeutic strategies targeting lipotoxic cell death in lipid-driven colorectal cancer.

MATERIALS AND METHODS

Cell Culture and Reagents

Human colorectal cancer cell lines HT29, HCT116, and RKO were cultured in McCoy's 5A (HT29 and HCT116 cells) or DMEM (RKO cell) medium supplemented with 10% fetal

bovine serum (FBS) and 1% penicillin–streptomycin at 37 °C with 5% CO_2. For lipid stress assays, cells were treated with palmitic acid (PA, 200 μM) or oleic acid (OA, 200 μM) complexed with fatty acid-free bovine serum albumin (BSA, 2:1 molar ratio). Atorvastatin (ATV, Solarbio), MS-444 (MedChemExpress), and actinomycin D (Sigma) were used at indicated concentrations.

Animal Models

All animal procedures were approved by the Institutional Animal Care and Use Committee (IACUC). ELAVL1$^{fl/fl}$ mice were crossed with Villin-Cre mice to generate intestinal epithelial cell-specific ELAVL1 conditional knockout mice. ELAVL1$^{fl/fl}$ littermates lacking Cre were used as controls. Genotypes were confirmed by PCR, and ELAVL1 deletion in intestinal epithelial or tumor tissues was verified by immunoblotting and IHC. Male C57BL/6J mice (6–8 weeks old) were treated with either a control diet (CD) or a high-fat diet (HFD, 60% kcal from fat) for 22 weeks. Colorectal tumorigenesis was induced by intraperitoneal injection of azoxymethane (AOM, 10-12.5 mg/kg, Sigma). In the HFD+AOM/DSS model, mice additionally received 2% dextran sodium sulfate (DSS) treatment in drinking water for three 5-day cycles. For therapeutic experiments, mice were randomly allocated into three groups, MS-444 (25 mg/kg, intraperitoneal, twice weekly) group, the ATV (10 mg/kg, oral gavage, daily) group, or a combination group starting at week 5. Tumor number, size, and colon length were recorded at sacrifice. Tissues were snap-frozen or formalin-fixed for downstream analyses.

Untargeted Lipidomics

Lipids were extracted from cell pellets using a modified Bligh–Dyer method and analyzed by LC-MS/MS (Thermo Q Exactive Plus). Data were processed using XCMS Online and LipidSearch software. Differential lipid species were identified using a fold-change ≥ 1.5 and $p < 0.05$. Pathway enrichment was performed using KEGG and MetaboAnalyst 5.0.

RNA Sequencing (RNA-seq)

Firstly, total RNA was isolated from HT29 cells expressing either shNC or shELAVL1. Sequencing libraries were generated using the NEBNext Ultra RNA Library Prep Kit and subjected to high-throughput sequencing on an Illumina NovaSeq 6000 platform. Clean reads were mapped to the human reference genome (GRCh38) with HISAT2. Differentially expressed genes were identified using DESeq2 with thresholds of $|log2FC| \geq 1$ and an adjusted P value < 0.05. Functional enrichment analyses, including Gene Ontology (GO) and KEGG pathway analyses, were performed using the clusterProfiler package.

RNA Immunoprecipitation (RIP-seq and RIP-qPCR)

RIP assays were performed using the PureBinding RNA Immunoprecipitation Kit (Geneseed) with an anti-ELAVL1 antibody or control IgG. Co-precipitated RNA was purified and analyzed by qRT-PCR or used for library construction and sequencing. Enrichment of HMGCR mRNA was calculated relative to input and normalized to IgG control.

RNA Pull-Down Assay

Biotinylated RNA probes corresponding to the 5′UTR, CDS, and 3′UTR of HMGCR mRNA were synthesized by in vitro transcription. Probes were incubated with recombinant ELAVL1 protein or HT29 cell lysates. RNA–protein complexes were captured using streptavidin magnetic beads and analyzed by Western blot using anti-ELAVL1 antibody.

Statistical Analysis

All data are presented as mean ± SD or SEM from at least three independent experiments. Statistical significance was determined using two-tailed Student's t-test for two groups or one-way/two-way ANOVA followed by Tukey's post hoc test for multiple comparisons. Correlations were assessed using Pearson's correlation coefficient. A p-value < 0.05 was considered statistically significant. All analyses were performed using GraphPad Prism 10.0.

ACKNOWLEDGEMENTS

Not applicable.

AUTHOR CONTRIBUTIONS

LL, ZQ, YH, HFX, and SY conceived and designed this study. HFX, SY, WYW, and ZRN carried out the experimental procedures and performed the associated bioinformatics analyses. HFX and ZRN were responsible for the collection of patient specimens and clinical data. LMT contributed to the bioinformatics investigation. LK and ZRN performed

the statistical evaluation. HFX and SY drafted the manuscript. HFX, SY, YH, ZQ, and LL participated in manuscript review and refinement. All authors reviewed the manuscript and gave final approval for publication.

COMPETING INTERESTS

The authors declare no competing interests.

DATA AVAILABILITY STATEMENT

The raw data supporting the conclusions of this article will be made available by the authors.

FUNDING

This study was supported by the Natural Science Foundation of Shanghai (Grant No. 25ZR1402580).

CONSENT FOR PUBLICATION

All of the authors consent for publication.

ETHICAL APPROVAL

Ethical Review and Animal Welfare: This study was approved by the Ethics Committee of Zhongnan Hospital, Wuhan University. All experimental procedures involving animals

were conducted in accordance with institutional regulations and the principles outlined in the Guidelines for the Care and Use of Laboratory Animals at Wuhan University (ZN2022042).

REFERENCES

1 Jin H-R, Wang J, Wang Z-J, Xi M-J, Xia B-H, Deng K *et al.* Lipid metabolic reprogramming in tumor microenvironment: from mechanisms to therapeutics. *J Hematol Oncol* 2023; **16**: 103.

2 Cheng C, Geng F, Cheng X, Guo D. Lipid metabolism reprogramming and its potential targets in cancer. *Cancer Commun (Lond)* 2018; **38**: 27.

3 Harayama T, Riezman H. Understanding the diversity of membrane lipid composition. *Nat Rev Mol Cell Biol* 2018; **19**: 281–296.

4 Li Z, Deng W, Yang L, Tang C, Yue J-M, Monteiro O *et al.* Lipid metabolism in homeostasis and disease. *Signal Transduct Target Ther* 2026; **11**: 55.

5 Jeon YG, Kim YY, Lee G, Kim JB. Physiological and pathological roles of lipogenesis. *Nat Metab* 2023; **5**: 735–759.

6 Zhang K-L, Zhu W-W, Wang S-H, Gao C, Pan J-J, Du Z-G *et al.* Organ-specific cholesterol metabolic aberration fuels liver metastasis of colorectal cancer. *Theranostics* 2021; **11**: 6560–6572.

7 Luo X, Cheng C, Tan Z, Li N, Tang M, Yang L *et al.* Emerging roles of lipid metabolism in cancer metastasis. *Mol Cancer* 2017; **16**: 76.

8 Snaebjornsson MT, Janaki-Raman S, Schulze A. Greasing the Wheels of the Cancer Machine: The Role of Lipid Metabolism in Cancer. *Cell Metab* 2020; **31**: 62–76.

9 Pundir CS, Narwal V. Biosensing methods for determination of triglycerides: A review. *Biosens Bioelectron* 2018; **100**: 214–227.

10 Mathiowetz AJ, Olzmann JA. Lipid droplets and cellular lipid flux. *Nat Cell Biol* 2024; **26**: 331–345.

11 Maestri A, Garagnani P, Pedrelli M, Hagberg CE, Parini P, Ehrenborg E. Lipid droplets, autophagy, and ageing: A cell-specific tale. *Ageing Res Rev* 2024; **94**: 102194.

12 Klemm RW, Carvalho P. Lipid Droplets Big and Small: Basic Mechanisms That Make Them All. *Annu Rev Cell Dev Biol* 2024; **40**: 143–168.

13 Olzmann JA, Carvalho P. Dynamics and functions of lipid droplets. *Nat Rev Mol Cell Biol* 2019; **20**: 137–155.

14 Cruz ALS, Barreto E de A, Fazolini NPB, Viola JPB, Bozza PT. Lipid droplets: platforms with multiple functions in cancer hallmarks. *Cell Death Dis* 2020; **11**: 105.

15 Petan T, Jarc E, Jusović M. Lipid Droplets in Cancer: Guardians of Fat in a Stressful World. *Molecules* 2018; **23**: 1941.

16 Scorletti E, Carr RM. A new perspective on NAFLD: Focusing on lipid droplets. *J Hepatol* 2022; **76**: 934–945.

17 Walther TC, Farese RV. Lipid droplets and cellular lipid metabolism. *Annu Rev Biochem* 2012; **81**: 687–714.

18 Valm AM, Cohen S, Legant WR, Melunis J, Hershberg U, Wait E *et al.* Applying systems-level spectral imaging and analysis to reveal the organelle interactome. *Nature* 2017; **546**: 162–167.

19 Cruz ALS, Barreto E de A, Fazolini NPB, Viola JPB, Bozza PT. Lipid droplets: platforms with multiple functions in cancer hallmarks. *Cell Death Dis* 2020; **11**: 105.

20 Prinz WA. Bridging the gap: membrane contact sites in signaling, metabolism, and organelle dynamics. *J Cell Biol* 2014; **205**: 759–769.

21 Hinman MN, Lou H. Diverse molecular functions of Hu proteins. *Cell Mol Life Sci* 2008; **65**: 3168–3181.

22 Matia-González AM, Laing EE, Gerber AP. Conserved mRNA-binding proteomes in eukaryotic organisms. *Nat Struct Mol Biol* 2015; **22**: 1027–1033.

23 Van Nostrand EL, Freese P, Pratt GA, Wang X, Wei X, Xiao R *et al.* A large-scale binding and functional map of human RNA-binding proteins. *Nature* 2020; **583**: 711–719.

24 Majumder M, Chakraborty P, Mohan S, Mehrotra S, Palanisamy V. HuR as a molecular target for cancer therapeutics and immune-related disorders. *Adv Drug Deliv Rev* 2022; **188**: 114442.

25 Wu X, Xu L. The RNA-binding protein HuR in human cancer: A friend or foe? *Adv Drug Deliv Rev* 2022; **184**: 114179.

26 Zhong L, Wu J, Zhou B, Kang J, Wang X, Ye F *et al.* ALYREF recruits ELAVL1 to promote colorectal tumorigenesis via facilitating RNA m5C recognition and nuclear export. *NPJ Precis Oncol* 2024; **8**: 243.

27 Huang F, Bu L, Li M, Wang Y, Zhang R, Shao Y *et al.* HuR/miR-124-3p/VDR complex bridges lipid metabolism and tumor development in colorectal cancer. *Carcinogenesis* 2025; **46**: bgae061.

28 Liu C, Lin Y, Wang Y, Lin S, Zhou J, Tang H *et al.* HuR promotes triglyceride synthesis and intestinal fat absorption. *Cell Rep* 2024; **43**: 114238.

29 Zhang J, Yang S, Wang J, Xu Y, Zhao H, Lei J *et al.* Equivalent carbon number-based targeted odd-chain fatty acyl lipidomics reveals triacylglycerol profiling in clinical colon cancer. *J Lipid Res* 2023; **64**: 100393.

30 Holmes B, Benavides-Serrato A, Freeman RS, Landon KA, Bashir T, Nishimura RN *et al.* mTORC2/AKT/HSF1/HuR constitute a feed-forward loop regulating Rictor expression and tumor growth in glioblastoma. *Oncogene* 2018; **37**: 732–743.

31 Zhang Z, Huang A, Zhang A, Zhou C. HuR promotes breast cancer cell proliferation and survival via binding to CDK3 mRNA. *Biomed Pharmacother* 2017; **91**: 788–795.

32 Balkhi MY, Iwenofu OH, Bakkar N, Ladner KJ, Chandler DS, Houghton PJ *et al.* miR-29 acts as a decoy in sarcomas to protect the tumor suppressor A20 mRNA from degradation by HuR. *Sci Signal* 2013; **6**: ra63.

33 Ghosh M, Aguila HL, Michaud J, Ai Y, Wu M-T, Hemmes A *et al.* Essential role of the RNA-binding protein HuR in progenitor cell survival in mice. *J Clin Invest* 2009; **119**: 3530–3543.

34 Li Z, Wang Y, Hu R, Xu R, Xu W. LncRNA B4GALT1-AS1 recruits HuR to promote osteosarcoma cells stemness and migration via enhancing YAP transcriptional activity. *Cell Prolif* 2018; **51**: e12504.

35 Tang H, Wang H, Cheng X, Fan X, Yang F, Zhang M *et al.* HuR regulates telomerase activity through TERC methylation. *Nat Commun* 2018; **9**: 2213.

36 Blanco FF, Jimbo M, Wulfkuhle J, Gallagher I, Deng J, Enyenihi L *et al.* The mRNA-binding protein HuR promotes hypoxia-induced chemoresistance through posttranscriptional regulation of the proto-oncogene PIM1 in pancreatic cancer cells. *Oncogene* 2016; **35**: 2529–2541.

37 Peng SS, Chen CY, Xu N, Shyu AB. RNA stabilization by the AU-rich element binding protein, HuR, an ELAV protein. *EMBO J* 1998; **17**: 3461–3470.

38 Sevinsky CJ, Khan F, Kokabee L, Darehshouri A, Maddipati KR, Conklin DS. NDRG1 regulates neutral lipid metabolism in breast cancer cells. *Breast Cancer Res* 2018; **20**: 55.

39 Liu X, Sun X, Mu W, Li Y, Bu W, Yang T *et al.* Autophagic flux-lipid droplet biogenesis cascade sustains mitochondrial fitness in colorectal cancer cells adapted to acidosis. *Cell Death Discov* 2025; **11**: 21.

40 Corbet C, Bastien E, Santiago de Jesus JP, Dierge E, Martherus R, Vander Linden C *et al.* TGFβ2-induced formation of lipid droplets supports acidosis-driven EMT and the metastatic spreading of cancer cells. *Nat Commun* 2020; **11**: 454.

41 Pakiet A, Sikora K, Kobiela J, Rostkowska O, Mika A, Sledzinski T. Alterations in complex lipids in tumor tissue of patients with colorectal cancer. *Lipids Health Dis* 2021; **20**: 85.

42 Cheng C, Geng F, Cheng X, Guo D. Lipid metabolism reprogramming and its potential targets in cancer. *Cancer Communications* 2018; **38**: 27.

43 Zadoorian A, Du X, Yang H. Lipid droplet biogenesis and functions in health and disease. *Nat Rev Endocrinol* 2023; **19**: 443–459.

44 Sterol synthesis pathway inhibition as a target for cancer treatment - PubMed. https://pubmed.ncbi.nlm.nih.gov/32711099/ (accessed 17 May2026).

45 Yeganeh B, Wiechec E, Ande SR, Sharma P, Moghadam AR, Post M *et al.* Targeting the mevalonate cascade as a new therapeutic approach in heart disease, cancer and pulmonary disease. *Pharmacol Ther* 2014; **143**: 87–110.

46 Li W, Xu J, Long Y, Zhang H, Rong X, Su Z. Emerging roles of the metabolic regulator 3-hydroxy-3-methylglutaryl coenzyme-CoA reductase in human cancers: From biology to therapeutics. *Genes Dis* 2026; **13**: 101945.

47 Dobrzycka M, Spychalski P, Łachiński AJ, Kobiela P, Jędrusik P, Kobiela J. Statins and Colorectal Cancer - A Systematic Review. *Exp Clin Endocrinol Diabetes* 2020; **128**: 255–262.

FIGURE

Figure 1

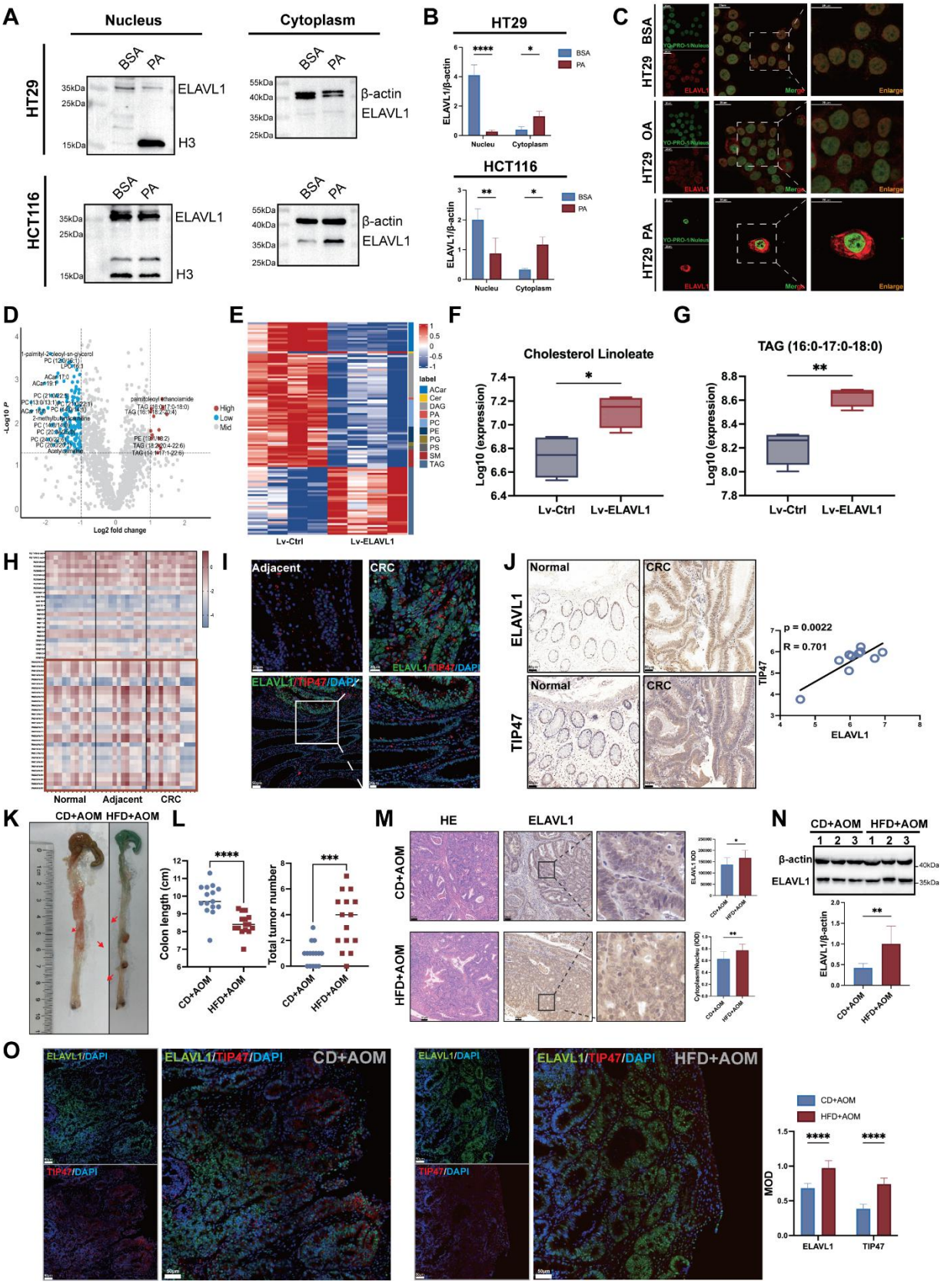

A
Nucleus
Cytoplasm
HT29
HCT116
BSA
PA
ELAVL1
H3
β-actin
35kDa
25kDa
15kDa
55kDa
40kDa
B
HT29
HCT116
ELAVL1/β-actin
Nucleu
Cytoplasm
C
YO-PRO-1/Nucleus
ELAVL1
Merge
Enlarge
D
Log2 fold change
-Log10 P
High
Low
Mid
E
Lv-Ctrl
Lv-ELAVL1
label
ACar
Cer
DAG
PA
PC
PE
PG
PS
SM
TAG
F
Cholesterol Linoleate
Log10 (expression)
G
TAG (16:0-17:0-18:0)
H
Normal
Adjacent
CRC
I
Adjacent
CRC
ELAVL1/TIP47/DAPI
J
Normal
CRC
ELAVL1
TIP47
p = 0.0022
R = 0.701
K
CD+AOM
HFD+AOM
L
Colon length (cm)
Total tumor number
M
HE
ELAVL1
CD+AOM
HFD+AOM
N
CD+AOM
HFD+AOM
β-actin
ELAVL1
40kDa
35kDa
O
ELAVL1/DAPI
TIP47/DAPI
ELAVL1/TIP47/DAPI
CD+AOM
HFD+AOM
MOD

Figure 1. Lipid stress induces cytoplasmic ELAVL1 accumulation and LD enrichment during CRC progression.

A–B. Cytoplasmic and nuclear ELAVL1 protein levels in HT29 and HCT116 cells after 24-h palmitate (PA) stimulation. Histone H3 and β-actin served as loading controls for nuclear and cytoplasmic fractions, respectively. Bar graphs show densitometric quantification (n = 3).

C. Representative immunofluorescence (IF) images of ELAVL1 in HT29 and HCT116 cells treated with PA or oleate (OA) for 24 h. Nuclei were counterstained with YO-PRO-1. Scale bar, 20 μm. n = 3.

D. Volcano plot of 1,335 differentially expressed lipid species identified by untargeted lipidomics after ELAVL1 overexpression (OE) in HT29 cells. Log2 fold-change and –log10 P values are shown.

E. Heat-map of 119 significantly altered lipid species. Fatty-acyl chains are separated by "/"; number before colon = carbon count, number after colon = double-bond number.

F-G. Violin plots of representative altered lipid classes.

H. Unsupervised heat-map of tissue lipidomes from 12 patients (normal mucosa, adjacent mucosa, CRC).

I. Dual-colour IF of ELAVL1 (green) and TIP47 (red) on serial sections of human CRC and adjacent mucosa. Left panel overview, scale bar 50 μm; right panel magnified, 20 μm; n = 10.

J. Representative immunohistochemistry (IHC) for ELAVL1 and TIP47 in CRC tissues with correlation analysis of staining intensity. Scale bar, 50 μm; n = 10.

K. Gross morphology of intestines from CD+AOM and HFD+AOM mice.

L. Colon length (left) and total tumour number (right) after 22-week HFD+AOM protocol. n = 15 mice per group.

M. ELAVL1 IHC in HFD+AOM colon sections. Scale bar, 50 μm. Bar graph quantifies cytoplasmic/nuclear integrated optical density (IOD) ratio.

N. Western blot (WB) validation of ELAVL1 in HFD+AOM colon lysates; n = 3.

O. IF co-staining of ELAVL1 (green) and TIP47 (red) in HFD+AOM intestines. Scale bar, 50 μm. n = 8.

ns $P \geq 0.05$, *$P < 0.05$, **$P < 0.01$, ***$P < 0.001$, ****$P < 0.0001$.

Figure 2

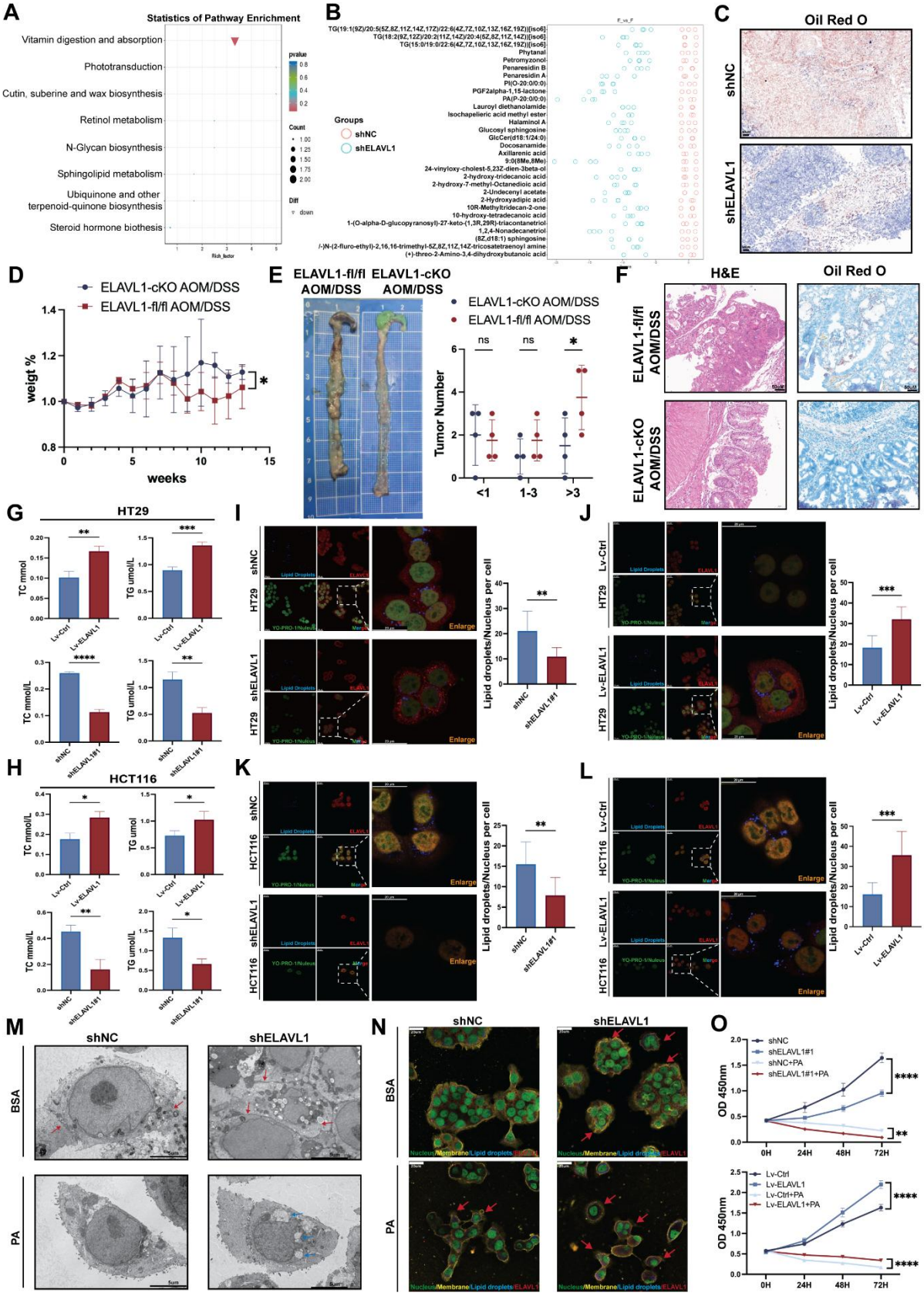

A
Statistics of Pathway Enrichment
Vitamin digestion and absorption
Phototransduction
Cutin, suberine and wax biosynthesis
Retinol metabolism
N-Glycan biosynthesis
Sphingolipid metabolism
Ubiquinone and other terpenoid-quinone biosynthesis
Steroid hormone biothesis
pvalue
Count
Diff
down
Rich_factor
B
Groups
shNC
shELAVL1
C
Oil Red O
shNC
shELAVL1
D
ELAVL1-cKO AOM/DSS
ELAVL1-fl/fl AOM/DSS
weigt %
weeks
E
ELAVL1-fl/fl AOM/DSS
ELAVL1-cKO AOM/DSS
ELAVL1-cKO AOM/DSS
ELAVL1-fl/fl AOM/DSS
Tumor Number
ns
ns
*
<1
1-3
>3
F
H&E
Oil Red O
ELAVL1-fl/fl AOM/DSS
ELAVL1-cKO AOM/DSS
G
HT29
TC mmol
TG umol/L
Lv-Ctrl
Lv-ELAVL1
shNC
shELAVL1#1
I
shNC
shELAVL1
HT29
Lipid Droplets
ELAVL1
YO-PRO-1/Nucleus
Merge
Enlarge
Lipid droplets/Nucleus per cell
J
Lv-Ctrl
Lv-ELAVL1
HT29
Lipid droplets/Nucleus per cell
H
HCT116
TC mmol/L
TG umol
K
HCT116
L
HCT116
M
shNC
shELAVL1
BSA
PA
N
shNC
shELAVL1
BSA
PA
Nucleus/Membrane/Lipid droplets/ELAVL1
O
shNC
shELAVL1#1
shNC+PA
shELAVL1#1+PA
OD 450nm
0H
24H
48H
72H
Lv-Ctrl
Lv-ELAVL1
Lv-Ctrl+PA
Lv-ELAVL1+PA

Figure 2. ELAVL1 protects CRC cells from lipid-overload-induced organelle injury and apoptosis.

A. KEGG enrichment bubble plot of differential lipids upon ELAVL1 knock-down.

B. Z-score bubble plot of top-30 altered lipid species of two groups (shELAVL1 vs shNC).

C. Oil-Red-O staining of subcutaneous xenografts (shELAVL1 vs shNC). Scale bar, 50 μm.

D. Body weight change of ELAVL1fl/fl and cKO mice during the induction of the AOM/DSS model.

E. Representative images of colonic tumors in ELAVL1fl/fl and cKO mice in the AOM/DSS model. Left: gross morphology of the colons; Right: statistical analysis of tumor size distributions (<1 mm, 1–3 mm, and >3 mm) between the two groups.

F. Representative images of H&E and Oil Red O staining from the two groups. Scale bar, 50 μm.

G-H. Total cholesterol (TC) and triglyceride (TG) quantification in HT29 and HCT116 cells: shNC, shELAVL1, Lv-Ctrl, Lv-ELAVL1. n = 3.

I–L. IF of ELAVL1 (red) and Lipid-droplet (blue) in HT29 (I, J) and HCT116 (K, L) cells after shELAVL1 or Lv-ELAVL1. Scale bars, 20 μm. n = 10.

M. Electron microscopy (EM) of HT29 plasma membrane after indicated treatments. Magnification ×8,000; scale bar, 5 μm.

N. Membrane dye staining in HT29 cells. Scale bar, 20 μm.

O. Growth curves of HT29 cells under PA stress with or without ELAVL1 modulation; n = 5.

ns $P \geqslant 0.05$, *$P < 0.05$, **$P < 0.01$, ***$P < 0.001$, ****$P < 0.0001$.

Figure 3

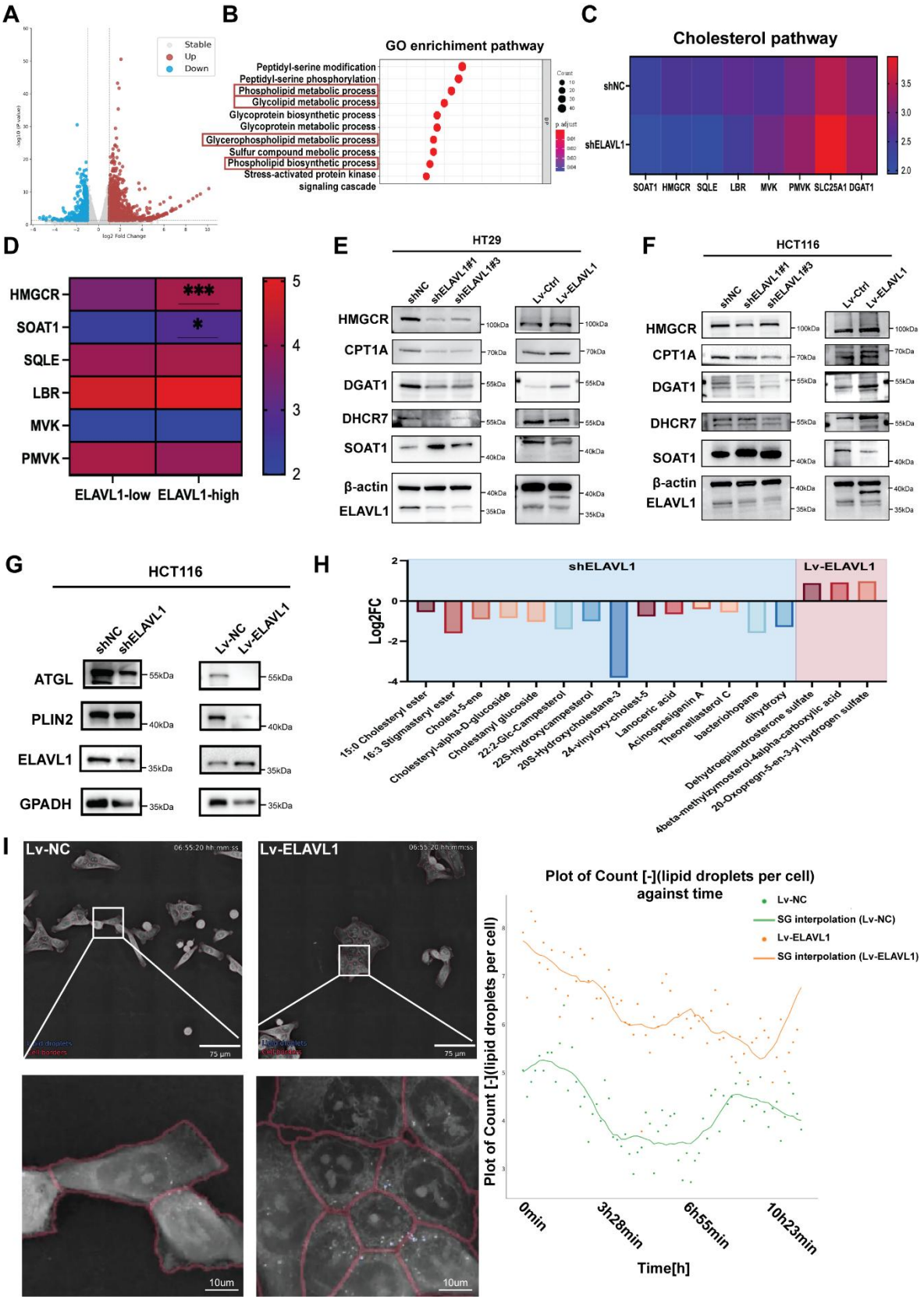

A
Stable
Up
Down
log2 Fold Change
B
GO enrichment pathway
Peptidyl-serine modification
Peptidyl-serine phosphorylation
Phospholipid metabolic process
Glycolipid metabolic process
Glycoprotein biosynthetic process
Glycoprotein metabolic process
Glycerophospholipid metabolic process
Sulfur compound metabolic process
Phospholipid biosynthetic process
Stress-activated protein kinase signaling cascade
C
Cholesterol pathway
shNC
shELAVL1
SOAT1 HMGCR SQLE LBR MVK PMVK SLC25A1 DGAT1
D
HMGCR
SOAT1
SQLE
LBR
MVK
PMVK
ELAVL1-low ELAVL1-high
E
HT29
shNC
shELAVL1#1
shELAVL1#3
Lv-Ctrl
Lv-ELAVL1
HMGCR
CPT1A
DGAT1
DHCR7
SOAT1
β-actin
ELAVL1
F
HCT116
G
HCT116
ATGL
PLIN2
ELAVL1
GPADH
H
shELAVL1
Lv-ELAVL1
Log2FC
15:0 Cholesteryl ester
16:3 Stigmasteryl ester
Cholest-5-ene
Cholesteryl-alpha-D-glucoside
Cholestanyl glucoside
22:2-Glc-Campesterol
22S-hydroxycampesterol
20S-Hydroxycholestane-3
24-vinyloxy-cholest-5
Lanoceric acid
Acinospesigenin A
Theonellasterol C
bacteriohopane
dihydroxy
Dehydroepiandrosterone sulfate
4beta-methylzymosterol-4alpha-carboxylic acid
20-Oxopregn-5-en-3-yl hydrogen sulfate
I
Lv-NC
Lv-ELAVL1
Plot of Count [-](lipid droplets per cell) against time
Lv-NC
SG interpolation (Lv-NC)
Lv-ELAVL1
SG interpolation (Lv-ELAVL1)
Plot of Count [-](lipid droplets per cell)
0min
3h28min
6h55min
10h23min
Time[h]

Figure 3. ELAVL1 promotes lipid droplet biogenesis and cholesterol-related biosynthesis centered on HMGCR.

A. Volcano plot showing differentially expressed genes (DEGs) in HT29 cells following ELAVL1 modulation (RNA-seq).

B. GO enrichment analysis of DEGs, highlighting the significant enrichment of cholesterol and lipid metabolism pathways.

C. qPCR analysis of key enzymes in the post-squalene cholesterol biosynthesis pathway (including HMGCR, SQLE, SOAT1, and LBR) in control (shNC) and ELAVL1-knockdown (shELAVL1) HT29 cells.

D. Clinical correlation analysis showing the association between ELAVL1 expression and levels of HMGCR and SOAT1 in CRC patient samples from Zhongnan Hospital.

E–F. Western blot analysis of key lipid-metabolic enzymes (HMGCR, CPT1A, DGAT1, DHCR7, SOAT1) and LD-associated proteins in HT29 (E) and HCT116 (F) cells after ELAVL1 modulation.

G. qPCR validation of lipogenic enzymes (DGAT1, DHCR7, SOAT1) and LD-associated genes (PLIN2, ATGL) following ELAVL1 alteration.

H. Untargeted lipidomics analysis (Heat-map) showing the alterations of specific cholesterol esters (CEs) and cholesterol-related metabolites in ELAVL1-knockdown or overexpressing cells.

I. Label-free live-cell imaging (Nanolive) and morphometric quantification of lipid droplet (LD) dynamics in Lv-NC and Lv-ELAVL1 cells over a 12-hour duration. The red lines mark the cell boundaries; the blue dots represent lipid droplets. Scale bars:75μm. Representative images (left) and the number of LDs per cell (right) are shown.

ns, P ⩾ 0.05; *P < 0.05; **P < 0.01; ***P < 0.001; ****P < 0.0001.

Figure 4

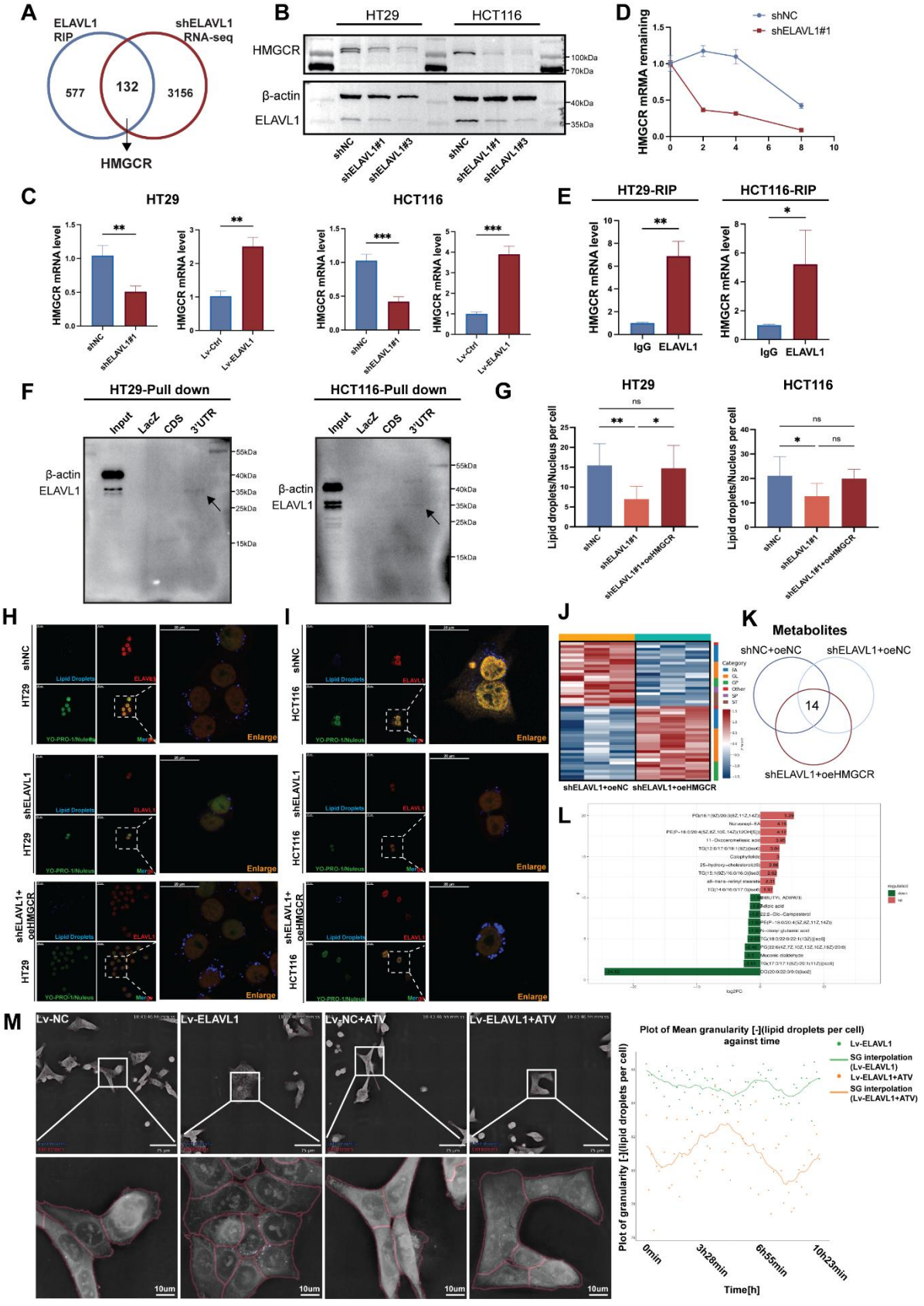

A
ELAVL1 RIP
shELAVL1 RNA-seq
577
132
3156
HMGCR
B
HT29
HCT116
HMGCR
β-actin
ELAVL1
100kDa
70kDa
40kDa
35kDa
shNC
shELAVL1#1
shELAVL1#3
D
shNC
shELAVL1#1
HMGCR mRNA remaining
C
HT29
HCT116
HMGCR mRNA level
Lv-Ctrl
Lv-ELAVL1
E
HT29-RIP
HCT116-RIP
IgG
ELAVL1
F
HT29-Pull down
HCT116-Pull down
Input
LacZ
CDS
3'UTR
55kDa
40kDa
35kDa
25kDa
15kDa
G
Lipid droplets/Nucleus per cell
shELAVL1#1+oeHMGCR
H
I
shNC
shELAVL1
shELAVL1+ oeHMGCR
HT29
HCT116
Lipid Droplets
ELAVL1
YO-PRO-1/Nucleus
Merge
Enlarge
J
shELAVL1+oeNC
shELAVL1+oeHMGCR
K
Metabolites
shNC+oeNC
shELAVL1+oeNC
14
shELAVL1+oeHMGCR
L
log2FC
M
Lv-NC
Lv-ELAVL1
Lv-NC+ATV
Lv-ELAVL1+ATV
Cytoplasm
Lipid droplets
Cell membrane
10um
Plot of Mean granularity [-](lipid droplets per cell) against time
Lv-ELAVL1
SG interpolation (Lv-ELAVL1)
Lv-ELAVL1+ATV
SG interpolation (Lv-ELAVL1+ATV)
Plot of granularity [-](lipid droplets per cell)
0min
3h28min
6h55min
10h23min
Time[h]

Figure 4. ELAVL1 directly stabilizes HMGCR mRNA to sustain LD buffering under lipid stress.

A. Venn diagram showing the intersection of ELAVL1-bound transcripts identified by RIP-seq and differentially expressed genes (DEGs) from RNA-seq in HT29 cells.

B–C. Validation of HMGCR expression. Western blot (B) and qPCR (C) analysis of HMGCR levels in HT29 and HCT116 cells following ELAVL1 knockdown or overexpression.

D. Actinomycin D chase (0–8 h) was performed to determine the half-life of HMGCR mRNA in control and ELAVL1-depleted HT29 cells.

E. RIP-qPCR analysis confirming the physical association and enrichment of HMGCR mRNA in ELAVL1 immunoprecipitates compared to IgG control. n=3.

F. Biotinylated RNA pull-down assay demonstrating that ELAVL1 protein selectively interacts with the 3′UTR of HMGCR mRNA, but not the 5′UTR or CDS.

G. Biochemical quantification of total cholesterol (TC) and triglycerides (TG) levels in HT29 cells across shNC, shELAVL1, and shELAVL1+oeHMGCR groups.

H–I. Rescue of lipid droplet (LD) phenotype. Representative immunofluorescence images and corresponding quantification of LD number and size in HT29 (H) and HCT116 (I) cells. The red lines mark the cell boundaries; the blue dots represent lipid droplets. Scale bar, 75 μm.

J. Heat-map showing the differential lipid profiles in shELAVL1 cells rescued with HMGCR (shELAVL1+oeNC vs. shELAVL1+oeHMGCR).

K. Venn diagram identifying 14 key lipid species whose abundance was restored by HMGCR re-expression.

L. Relative abundance of the 14 identified lipid species (including TGs, PCs, and CEs) across the indicated groups.

M. Label-free live-cell imaging (Nanolive) and morphometric quantification of lipid droplet (LD) dynamics in Lv-NC, Lv-ELAVL1, Lv-NC+ATV and Lv-ELAVL1+ATV cells over a 12-hour duration. Scale bars:75μm. Representative images (left) and the number of LDs per cell (right) are shown.

ns $P \geqslant 0.05$, *$P < 0.05$, **$P < 0.01$, ***$P < 0.001$, ****$P < 0.0001$.

Figure 5

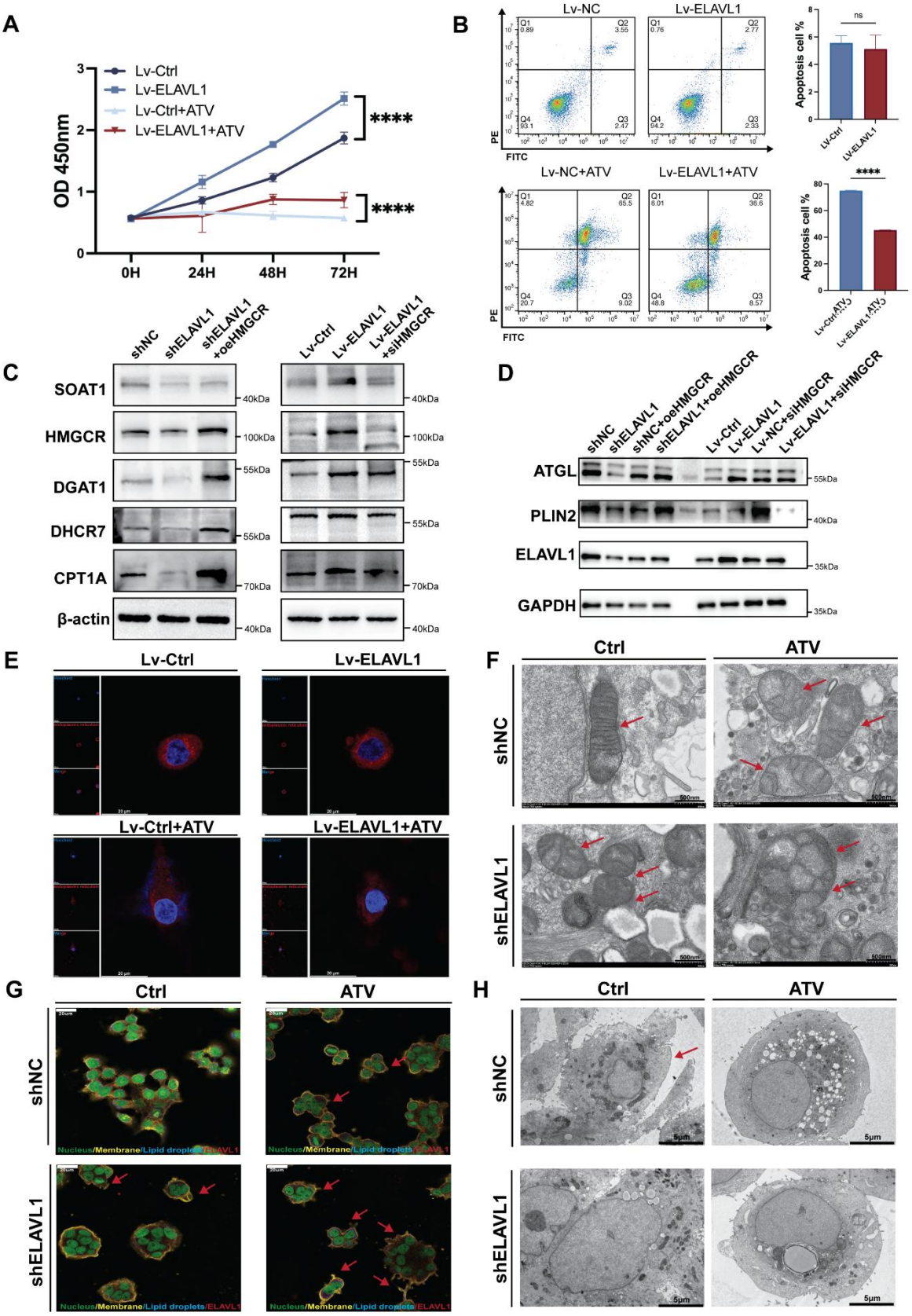

A
Lv-Ctrl
Lv-ELAVL1
Lv-Ctrl+ATV
Lv-ELAVL1+ATV
OD 450nm
****
****
0H
24H
48H
72H
B
Lv-NC
Lv-ELAVL1
Lv-NC+ATV
Lv-ELAVL1+ATV
PE
FITC
Apoptosis cell %
ns
****
C
shNC
shELAVL1
shELAVL1 +oeHMGCR
Lv-Ctrl
Lv-ELAVL1
Lv-ELAVL1 +siHMGCR
SOAT1
HMGCR
DGAT1
DHCR7
CPT1A
β-actin
D
shNC
shELAVL1
shNC+oeHMGCR
shELAVL1+oeHMGCR
Lv-Ctrl
Lv-ELAVL1
Lv-NC+siHMGCR
Lv-ELAVL1+siHMGCR
ATGL
PLIN2
ELAVL1
GAPDH
E
Lv-Ctrl
Lv-ELAVL1
Lv-Ctrl+ATV
Lv-ELAVL1+ATV
F
Ctrl
ATV
shNC
shELAVL1
G
Ctrl
ATV
shNC
shELAVL1
Nucleus/Membrane/Lipid droplets/ELAVL1
H
Ctrl
ATV
shNC
shELAVL1
5μm

Figure 5. The ELAVL1–HMGCR axis prevents lipotoxic organelle damage and apoptosis.

A. CCK-8 viability of HT29 cells for groups: Lv-Ctrl, Lv-ELAVL1 with or without atorvastatin (ATV).

B. Apoptosis assay for groups: Lv-Ctrl, Lv-ELAVL1 with or without ATV.

C. WB of metabolic enzymes and apoptosis markers of shNC, shELAVL1, shELAVL1+oeHMGCR, Lv-NC, Lv-ELAVL1, and Lv-ELAVL1+siHMGCR groups in HT29 cells.

D. WB of lipid droplets-related enzymes of shNC, shELAVL1, shNC+oeHMGCR, shELAVL1+oeHMGCR, Lv-NC, Lv-ELAVL1, Lv-NC+siHMGCR, and Lv-ELAVL1+siHMGCR groups in HT29 cells.

E. ER-Tracker staining in HT29 cells for groups: Lv-Ctrl, Lv-ELAVL1 with or without atorvastatin (ATV). Scale bar, 20 μm.

F. EM images of mitochondrial morphology. Magnification ×20,000; scale bars 500 nm.

G. DiD membrane staining by confocal microscopy. Scale bar, 20 μm.

H. EM images of plasma-membrane morphology. Magnification ×8,000; scale bars 5 μm.

ns $P \geqslant 0.05$, *$P < 0.05$, **$P < 0.01$, ***$P < 0.001$, ****$P < 0.0001$.

Figure 6

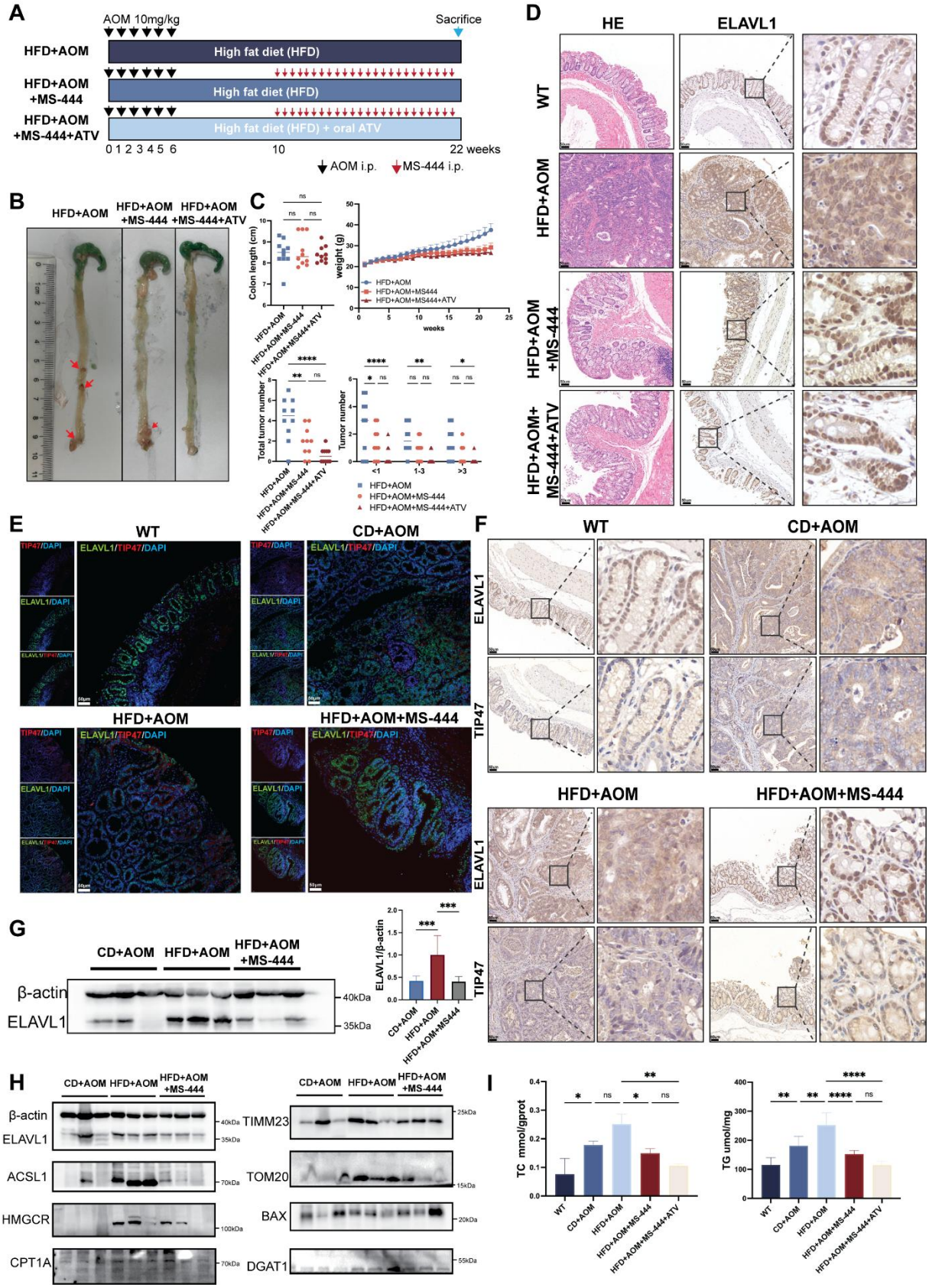

A
AOM 10mg/kg
Sacrifice
HFD+AOM
High fat diet (HFD)
HFD+AOM +MS-444
High fat diet (HFD)
HFD+AOM +MS-444+ATV
High fat diet (HFD) + oral ATV
0 1 2 3 4 5 6
10
22 weeks
AOM i.p.
MS-444 i.p.
B
HFD+AOM
HFD+AOM +MS-444
HFD+AOM +MS-444+ATV
C
Colon length (cm)
weight (g)
weeks
HFD+AOM
HFD+AOM+MS444
HFD+AOM+MS444+ATV
Total tumor number
Tumor number
<1
1-3
>3
D
HE
ELAVL1
WT
HFD+AOM
HFD+AOM +MS-444
HFD+AOM+ MS-444+ATV
E
WT
CD+AOM
HFD+AOM
HFD+AOM+MS-444
TIP47/DAPI
ELAVL1/DAPI
ELAVL1/TIP47/DAPI
F
WT
CD+AOM
HFD+AOM
HFD+AOM+MS-444
ELAVL1
TIP47
G
CD+AOM
HFD+AOM
HFD+AOM +MS-444
β-actin
ELAVL1
40kDa
35kDa
ELAVL1/β-actin
H
CD+AOM
HFD+AOM
HFD+AOM +MS-444
β-actin
ELAVL1
ACSL1
HMGCR
CPT1A
TIMM23
TOM20
BAX
DGAT1
I
TC mmol/gprot
TG umol/mg
WT
CD+AOM
HFD+AOM
HFD+AOM+MS-444
HFD+AOM+MS-444+ATV

Figure 6. Combined targeting of ELAVL1 and HMGCR disrupts lipid homeostasis and suppresses lipid-driven CRC.

A. Drug-intervention timeline in HFD+AOM mice.

B. Gross intestinal images from HFD+AOM, HFD+AOM+MS-444, and HFD+AOM+MS-444+ATV groups.

C. Colon length, body weight, tumour counts, and size distribution after 22 weeks. n = 10.

D. HE and IHC for ELAVL1 in WT, HFD+AOM, HFD+AOM+MS-444, and HFD+AOM+MS-444+ATV colons. Scale bar, 50 μm.

E–F. IF (E) and IHC (F) co-staining of ELAVL1 and TIP47 in mouse colons. Scale bar, 50 μm

G. WB validation of ELAVL1 in treated groups.

H. WB profiling of metabolic enzymes, mitochondrial markers (TIMM23, TOM20) and apoptosis regulator BAX in colon lysates. n = 3.

I. Tissue TC (left) and TG (right) levels across genotypes and treatments. n = 5.

ns $P \geqslant 0.05$, *$P < 0.05$, **$P < 0.01$, ***$P < 0.001$, ****$P < 0.0001$.

Supplementary Files

This is a list of supplementary files associated with this preprint. Click to download.

- SupplementaryMaterials1.pdf
- SupplementaryMaterials2WB.pdf